Flow, Turbulence and Combustion
https://doi.org/10.1007/s10494-025-00687-y

RESEARCH

Quantitative Flow Visualization of Underexpanded Elliptic Jets by Rainbow Schlieren Tomography

Takumi Sakashita[1] · **Tatsuya Nagata**[1] · **Shinichiro Nakao**[1] · **Yoshiaki Miyazato**[1]

Received: 14 March 2025 / Accepted: 24 July 2025

Abstract

The underexpanded jet issuing from an elliptic convergent nozzle with an aspect ratio of 8 is quantitatively visualized using rainbow schlieren tomography. Flow visualizations are conducted at a nozzle pressure ratio of 4.0 to produce strong shocks within the jet plume. The Reynolds number, based on the equivalent diameter and flow properties at the nozzle exit, is 4.0×10^5. Multi-view rainbow schlieren images with a horizontal filter setting are captured by rotating the nozzle around its central axis at an angular step of 5°, ranging from 0° to 180°. The jet density field is reconstructed at a spatial resolution of 13 μm using the convolution back projection method. The near-field flow features of a shock-containing elliptic jet with a high aspect ratio are experimentally demonstrated for the first time. In addition, to examine the effects of angular steps on the reconstructed density field, the rainbow schlieren images taken at 10°, 20°, and 30° intervals are selected from a total of 37 rainbow schlieren images captured at 5° intervals. The density field is then reconstructed for these specific angular steps. The effects of angular steps are clarified on the two-dimensional density fields in the minor-axis and major-axis planes, as well as on the streamwise density profiles along the jet centerline and liplines in both the minor-axis and major-axis planes.

Keywords Density measurement · Elliptic nozzle · Rainbow schlieren tomography · Shock wave · Underexpanded jet

---

Tatsuya Nagata, Shinichiro Nakao and Yoshiaki Miyazato contributed equally to this work.

✉ Yoshiaki Miyazato
miyazato@kitakyu-u.ac.jp

Takumi Sakashita
sakataku66@gmail.com

Tatsuya Nagata
ntatsuya120122@gmail.com

Shinichiro Nakao
s-nakao@kitakyu-u.ac.jp

[1] Department of Mechanical Systems Engineering, The University of Kitakyushu, 1-1 Hibikino, Wakamatsu-Ku, Kitakyushu, Fukuoka 808-0135, Japan

1 Introduction

Elliptic nozzles are widely recognized for their numerous advantages over conventional round and rectangular nozzles, including improved flow mixing within the supersonic jet, shorter potential core length, enhanced shear layer entrainment, and reduced shock-associated noise under specific operating conditions (Kinzie and McLaughlin 1999). It suggests that elliptic nozzles are effective as a passive flow control strategy. However, previous studies on shock-containing elliptic jets have focused primarily on aspects related to shock-associated noise, such as screech tones. Few studies have examined the characteristics of the region within the elliptic jet where shock waves are dominant, despite the engineering and academic importance of understanding the three-dimensional flow characteristics of shock-containing elliptic jets (Edgington-Mitchell 2019).

The flow characteristics in regions dominated by shock waves within underexpanded elliptical jets have been experimentally studied by Mitchell et al. (Mitchell et al. 2013), Edgington-Mitchell et al. (Edgington-Mitchell et al. 2015b, 2015a), Perumal et al. (Perumal and Rathakrishnan 2021), Nagata et al. (Nagata et al. 2024), and Mazharmanesh et al. (Mazharmanesh et al. 2025). Mitchell et al. (Mitchell et al. 2013) investigated the near-field structure of underexpanded jets issuing from an elliptic convergent nozzle with an aspect ratio (AR) of 2 and nozzle pressure ratios (NPRs) of 2.2, 2.6, 3.4, and 4.2 using high-resolution planar particle image velocimetry (PIV) where AR is defined as the ratio of the major axis length to the minor axis length at the nozzle exit face, while NPR is defined as the ratio of the stagnation pressure upstream of the nozzle to the back pressure. They displayed an axis-switching phenomenon typical of asymmetric jets. Edington-Mitchell et al. (Edgington-Mitchell et al. 2015b, 2015a) examined staging behavior in screeching elliptic jets based on the frequency of the dominant screech tone. Perumal et al. (Perumal and Rathakrishnan 2021) conducted experiments using Pitot tubes to measure overexpanded and underexpanded jets issuing from circular and elliptic nozzles. By compiling these experimental results along with previous research findings, they proposed a semi-empirical law for the supersonic length (Tashiro et al. 2023) of circular and elliptical jets with shock waves. Nagata et al. (Nagata et al. 2024) quantitatively measured the density field of an underexpanded jet emerging from an elliptic convergent nozzle with $AR=4$ under a condition of $NPR=4$ using rainbow schlieren tomography (RST) and elucidated the streamwise location of the axis-switching, the supersonic length, and the three-dimensional structure of shock waves within the jet. Mazharmanesh et al. (Mazharmanesh et al. 2025) identified a quasi-helical mode in an elliptic jet by analyzing ultra-high-speed schlieren images, employing spectral proper orthogonal decomposition (SPOD).

Some studies numerically explored the characteristics of shock-containing elliptic jets (Menon and Skews 2010; Li et al. 2017). Menon and Skews (Menon and Skews 2010) investigated the characteristics of underexpanded jets issuing from elliptic convergent nozzles with ARs of 2 and 4 by solving the Reynolds-averaged Navier-Stokes (RANS) equations and using shadowgraph techniques. Li et al. (Li et al. 2017) numerically demonstrated steady and unsteady flow characteristics of an underexpanded jet issuing from an elliptic convergent nozzle with $AR=2$ at $NPR=5.6$ using large eddy simulation (LES). However, to the best of the authors' knowledge, the experimental datasets necessary to validate computational codes are insufficient. As a result, the validation process is typically conducted qualitatively by comparing the results with schlieren or shadowgraph images or by leveraging experimental data from prior investigations on shock-containing round jets. On the other hand, in the absence of strong shock waves, such as Mach stems, within elliptic jets, the governing equations of the flow field can often be simplified. Utilizing this simplification, several studies have analytically investigated the fundamental structure of the shock-containing elliptic jet. Nagata et al. (Nagata et al. 2022) proposed a flow model to analytically evaluate the effects of NPR and AR on the shock-cell length. Their model can quantitatively predict previous experimental shock-cell lengths. Islam et al. (Islam et al. 2024) introduced an analytical model for shock-containing elliptic jets under slightly off-design conditions. Ivelja et al. (Ivelja et al. 2024) developed comprehensive models to describe the behavior of both upstream- and downstream-traveling waves in screeching elliptic jets by applying proper orthogonal decomposition (POD) to experimental velocity data collected from both the major and minor axis planes of underexpanded elliptic jets.

Quantifying regions dominated by shock waves presents significant experimental challenges. When intrusive probes such as Pitot tubes and hotwire anemometers are employed to measure physical quantities within supersonic jets, several challenges arise. For instance, the measured value does not represent the true total pressure of the flow, as a bow shock forms ahead of the probe in supersonic flows (Katanoda et al. 2000), leading to a reduction in total pressure. Additionally, the presence of shocks can introduce significant measurement errors, particularly in regions where the flow transitions from supersonic to subsonic. Furthermore, the insertion of the probe into the flow can disrupt the flow field, thereby altering the characteristics of the jet being measured. These issues necessitate meticulous consideration and calibration when using Pitot tubes for supersonic flow measurements.

The application of optical diagnostic techniques using tracer particles, such as laser Doppler anemometry (LDA), particle image velocimetry (PIV), and laser-induced fluorescence (LIF), to measure physical quantities within supersonic jets presents several significant challenges [(Yoo et al. 2010; Feng and McGuirk 2016; Sakurai et al. 2015; Yüceil 2017)]. Firstly, ensuring that tracer particles accurately and promptly follow the flow dynamics is particularly difficult in regions where the flow transitions rapidly from supersonic to subsonic before and after a strong shock wave. Secondly, discrepancies between the dimensions and density of the tracer particles and the fluid can lead to erroneous measurements, as the particles may not perfectly mimic the fluid's motion. In contrast, in recent years, there has been an increasing use of visualization techniques that exploit the property of light's refractive index being a function of density alone to investigate the density fields in shock-dominated flows. Laser interferometry, which leverages the principle that light travels at different speeds through regions of varying density, has been extensively used. Sugawara et al. (Sugawara et al. 2020, 2021) quantitatively elucidated the flow characteristics in the near-field of underexpanded round microjets using Mach-Zehnder interferometry (MZI). Similarly, Leon et al. (Léon et al. 2022) revealed the three-dimensional structure of a screeching underexpanded jet in helical mode using multi-view digital holographic interferometry. Recently, Yoshimi et al. (Yoshimi et al. 2025) elucidated the three-dimensional structure of shock waves within the underexpanded jet issuing from a micro rectangular convergent nozzle with a high aspect ratio using MZI. However, laser interferometry requires expensive optical components such as beam splitters and lasers, and the setup demands skilled techniques. On the other hand, there are visualization techniques based on the schlieren principle, which are cost-effective and simpler to set up.

Schlieren methods (Settles 2001) exploit the refraction of light passing through regions with density gradients. Notable examples include background-oriented schlieren (BOS) (Settles and Hargather 2017) and rainbow schlieren deflectometry (RSD) (Agrawal and Wanstall 2018). However, despite its advantages, BOS can be limited in terms of spatial resolution. This limitation arises because the cameras are focused on the background rather than the flow of interest. Additionally, spatial filtering induced by image correlation algorithms further contributes to this constraint (Léon et al. 2022). On the other hand, RSD is recognized for its high spatial resolution and has been successfully applied to underexpanded round jets (Tashiro et al. 2023; Takano et al. 2016; Maeda et al. 2018), underexpanded rectangular jets (Fukunaga et al. 2022), and underexpanded elliptic jets (Nagata et al. 2024).

The present study is motivated by the lack of an experimental dataset needed to validate numerical simulations and analytical models on shock-containing elliptic jets. In our previous study (Nagata et al. 2024), the flow topology and shock structure in the near-field region of an underexpanded jet emerging from an elliptic convergent nozzle with an aspect ratio of 4, operating at a nozzle pressure ratio of 4, were quantitatively elucidated. To the best of the authors' knowledge, the only experimental study on shock-containing elliptic jets with a high AR is performed by Rao et al. (Rao et al. 2020), who investigated an underexpanded jet issuing from an elliptic convergent nozzle with AR = around 8 using high-speed schlieren imaging and acoustic measurements. However, their research primarily concentrated on the feedback mechanism of screech tones, thus the internal structure of the jets remains unexamined. Therefore, the present study examines the three-dimensional flow characteristics of the shock-dominated region in an underexpanded jet emerging from an elliptic convergent nozzle with AR = 8.

2 Experimental Methods

2.1 Measurement System and Test Nozzle

The experiments were conducted in an intermittent blowdown compressed-air facility. Since the facility has been described in detail elsewhere (Nagata et al. 2024), only a brief description is given in the present paper. The ambient air is pressurized by the compressor up to 1 MPa and stored in a high-pressure reservoir comprising two storage tanks with a total capacity of 2 m^3 after filtering and drying. The high-pressure dry air from the reservoir stagnates in the plenum chamber through a coupling as shown in Fig. 1. Subsequently, it is discharged into the quiescent air through the test nozzle that can be rotated about its central axis (Nagata et al. 2024). The desired nozzle pressure ratio (NPR $= p_{os}/p_b$) is achieved by changing the plenum pressure, p_{os}, with the back pressure, p_b, held constant at 4.0 within an accuracy of 1.0 $\%$. In the present experiments, p_b is 101.8 kPa $\pm$ 0.5 kPa and the ambient temperature T_b is 299.8 K $\pm$ 0.1 K. As shown in Fig. 2, an elliptic convergent nozzle with an AR of 8 is used as a test nozzle where the AR is defined as the ratio (L_a/L_b) of the semi-major length ($L_a = 10$ mm) to the semi-minor length ($L_b = 1.25$) at the nozzle exit. The equivalent diameter (Nagata et al. 2022) at the nozzle exit is given by $D_{eq} = 2(L_a L_b)^{1/2}$ and it becomes approximately 7.1 mm for the present nozzle. The Reynolds number, based upon the equivalent diameter and flow properties at the nozzle exit, is 4.01 $\times$ 10^5.

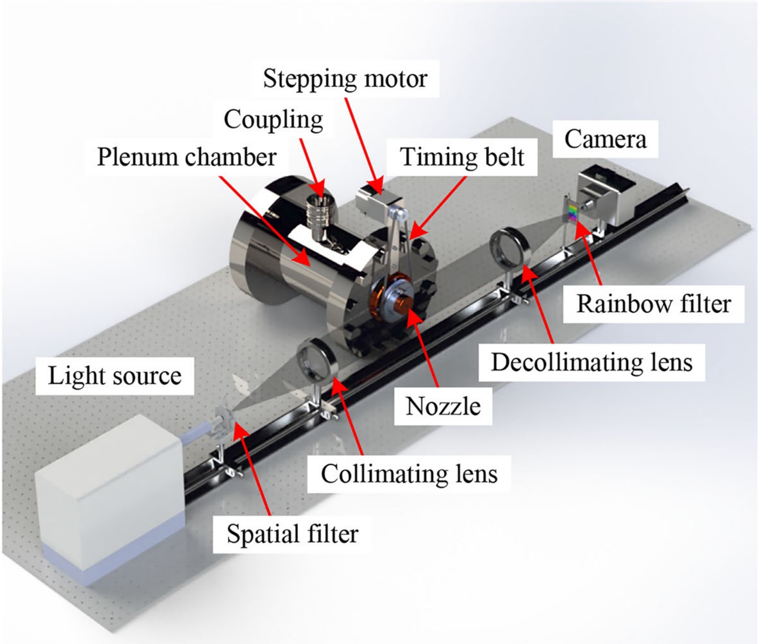

Fig. 1 Schematic diagram of the experimental apparatus with a rainbow schlieren optical system. High-pressure dry air is supplied to the plenum chamber through the coupling and then discharged into the atmosphere through the test nozzle

Fig. 2 Cut-model of a test nozzle and the Cartesian coordinate system (x, y, z) with its origin at the center of the nozzle exit plane. The x, y, and z are measured from the origin along the major axis, minor axis, and center axis of the nozzle, respectively

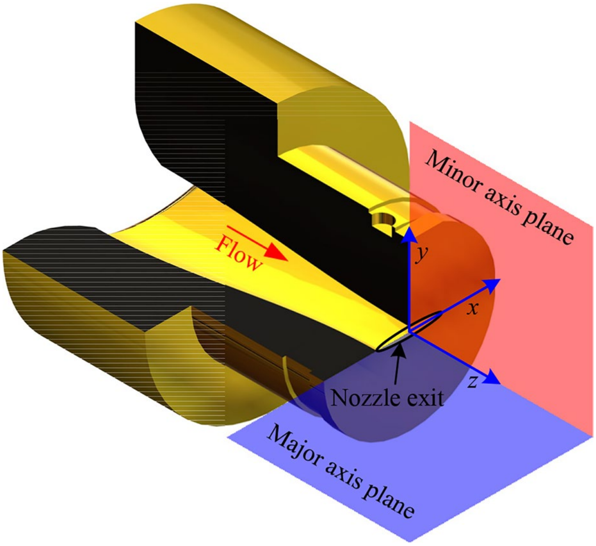

The nozzle was fabricated using a 3D printer (Flashforge, Adventurer 3X) employing fused deposition modeling (FDM). This method utilizes melt extrusion to deposit thermoplastic filaments according to a predetermined pattern. The geometry of the nozzle exit and the internal wall roughness significantly influence the flow characteristics of the jets issuing from the nozzle. To investigate these features, a digital image of the nozzle exit was captured using a laser scanning microscope (Olympus, LEXT OLS4100), and the wall shape was measured as a function of the polar angle, θ, as depicted in Fig. 3. The red line represents the designed elliptic curve, while the open symbols denote the measured values. The design curve and the measurement data exhibit excellent quantitative agreement, with a standard deviation of approximately 11 μm. Additionally, the arithmetic mean roughness, R_a, of the internal nozzle wall was measured using a surface roughness measuring machine (Mitutoyo, SV-C524) with a resolution of 0.05 μm in both vertical and horizontal directions, yielding a value of 6.37 μm.

2.2 Rainbow Schlieren Tomography

Quantitative flow visualizations of shock-containing elliptic jets were carried out by the rainbow schlieren tomography (RST) (Nagata et al. 2024). In this study, an in-house rainbow filter with 4.4 mm in width and 35 mm in length was utilized. An image of the rainbow filter, along with its calibration curve, is presented in Fig. 4(a). In the HSI color representation, the hue (color) of the rainbow filter transitions continuously from the left to the right end, with a physical quantity ranging from 0 to 360 ° assigned to the hue at each position. In the present experiment, a single parameter H, represented by an 8-bit image (256 gradation levels), is assigned to the width (4.4 mm) of the rainbow filter. This implies that the filter resolution is approximately 17 μm, which is about one-third the size (50 μm) of the light source image projected onto the rainbow filter.

Similar to the traditional greyscale schlieren method using a knife-edge, the rainbow filter is installed horizontally in the schlieren cutoff plane. Before starting the experiment,

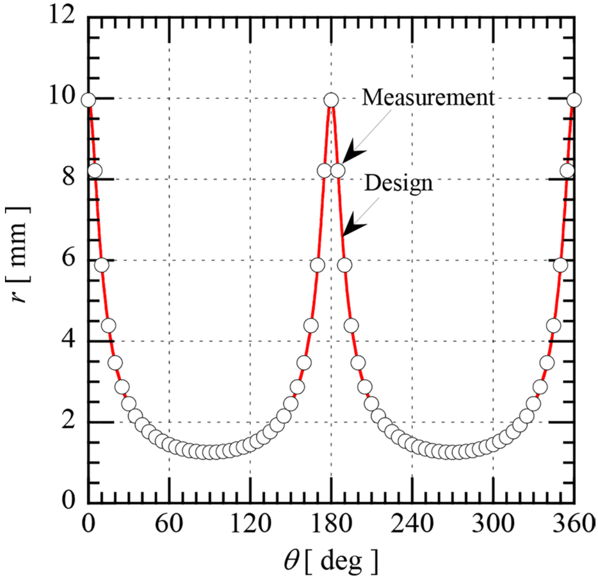

Fig. 3 Wall shape at the nozzle exit section against the polar angle. The red line denotes the design curve for an ellipse with semi-major and semi-minor lengths of $L_a = 10$ mm and $L_b = 1.25$ mm, respectively, and the open symbols are measured values

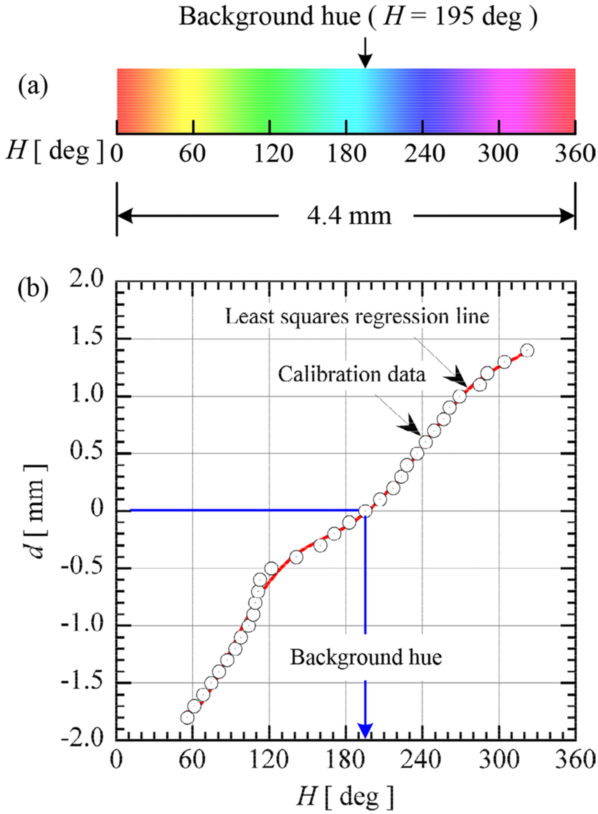

Fig. 4 Calibration characteristics of a rainbow filter. (**a**) An image of rainbow filter and (**b**) calibration data with the least squares regression line and a background hue of 195 deg. The approximation curve is a fifth-degree polynomial

the filter is moved in 10 μm increments from a reference position in the direction where the hue changes. This allows the camera's sensor to record specific colors based on the filter's movement, enabling the creation of a calibration curve for the rainbow filter, as shown in Fig. 4(b). The open symbols represent the calibration data with a maximum precision error of approximately 3° in the hue values. The solid line indicates a least squares regression curve of the calibration data, which is represented by a fifth-order polynomial. The background hue in the rainbow filter for the present experiment corresponds to the location indicated by the blue arrow. Detailed procedures for designing, generating, and calibrating a rainbow filter are described in Agrawal and Wanstall (Agrawal and Wanstall 2018). The jet density field is reconstructed using the convolution back projection (CBP) technique. The present rainbow schlieren system has a spatial resolution of 13 μm in the object plane, which can be evaluated based on the physical and image dimensions of the test nozzle (Kolhe and Agrawal 2009). The method for reconstructing three-dimensional density fields using RST is comprehensively detailed in our most recent publication (Nagata et al. 2024); therefore, it is not elaborated upon in this context.

When reconstructing the three-dimensional density field of an asymmetric jet using the CBP method, the optimal angular step for capturing images around the jet's central axis is not known in advance. Generally, a smaller angular step results in higher accuracy of the reconstructed density field but requires a larger number of images. Therefore, it is necessary to select a larger angular step within a tolerable range to balance accuracy and practicality.

In this study, an angular step ($\Delta\theta$) of 5° was set, and multi-directional imaging of the jet was conducted, resulting in a total of 37 captured images. Subsequently, images corresponding to $\Delta\theta$ values of 5°, 10°, and 20° were selected from this dataset. Using the CBP method, the density field of the jet was reconstructed, and the effects of $\Delta\theta$ on the reconstructed density field were examined.

Furthermore, before the density field of the jet is reconstructed, three typical filtering processes including bilateral filter, block-matching and 3D (BM3D) filter, and total variation (TV) filter were applied to the rainbow schlieren images. The bilateral filter is a non-linear, edge-preserving, and noise-reducing smoothing filter for images and it preserves sharp edges. The BM3D filter is a 3-D block-matching algorithm used primarily for noise reduction in images. The TV filter is based on the principle that signals with excessive and possibly spurious detail have a high total variation.

In our preliminary study (Sakashita et al. 2024), the effects of three image filters on the streamwise density profiles along typical locations: the central axis, the lipline in the minor-axis plane, and the lipline in the major-axis plane of an underexpanded elliptic jet were examined. The TV filter was found to be the most effective. Consequently, in the present study, only the TV filter was utilized.

3 Results and Discussion

3.1 Flow Visualization

Rainbow schlieren pictures of an underexpanded elliptic jet are shown in Fig. 5 with flow from left to right. The downstream distance (z) from the nozzle exit and its dimensionless distance (z/D_{eq}) are indicated below the picture for reference. To observe changes in the density gradient perpendicular to the flow direction, the rainbow filter is placed parallel to the flow in the schlieren cut-off plane. The color of the schlieren images corresponds to the hue value of the rainbow filter shown at the right of Fig. 5. The magnitude of the density gradient is proportional to the difference from the background hue ($H = 195°$). In regions along the jet's central axis and sufficiently far from the jet's central axis, the density gradient is zero, resulting in the hue value matching the background hue value. In regions where the density gradient in the y-direction is positive ($\partial\rho/\partial y > 0$), the hue value is smaller than that of the background hue ($H = 195°$), and the greater the absolute value of the density gradient, the smaller the hue value becomes. In contrast, in regions where the density gradient in the y-direction is negative ($\partial\rho/\partial y < 0$), the hue value is greater than that of the background hue, and the greater the absolute value of the density gradient, the larger the hue value becomes. In Fig. 5(a), observing the jet boundary immediately downstream of the nozzle exit, the upper jet boundary is purple, while the lower jet boundary is yellow. From this, it can be inferred that at the upper jet boundary, $\partial\rho/\partial y < 0$, and at the lower jet boundary, $\partial\rho/\partial y > 0$.

From Fig. 5(a), which shows the minor-axis plane view, the jet exiting the nozzle initially spreads radially due to underexpansion but contracts toward the location of the first shock just downstream of the nozzle to form the first shock-cell. A second shock is faintly visible downstream of the first shock but is obscured by the flow oscillations (Rao et al. 2020). In Fig. 5(b), which shows the major-axis plane view, the first shock can be seen to form a cres-

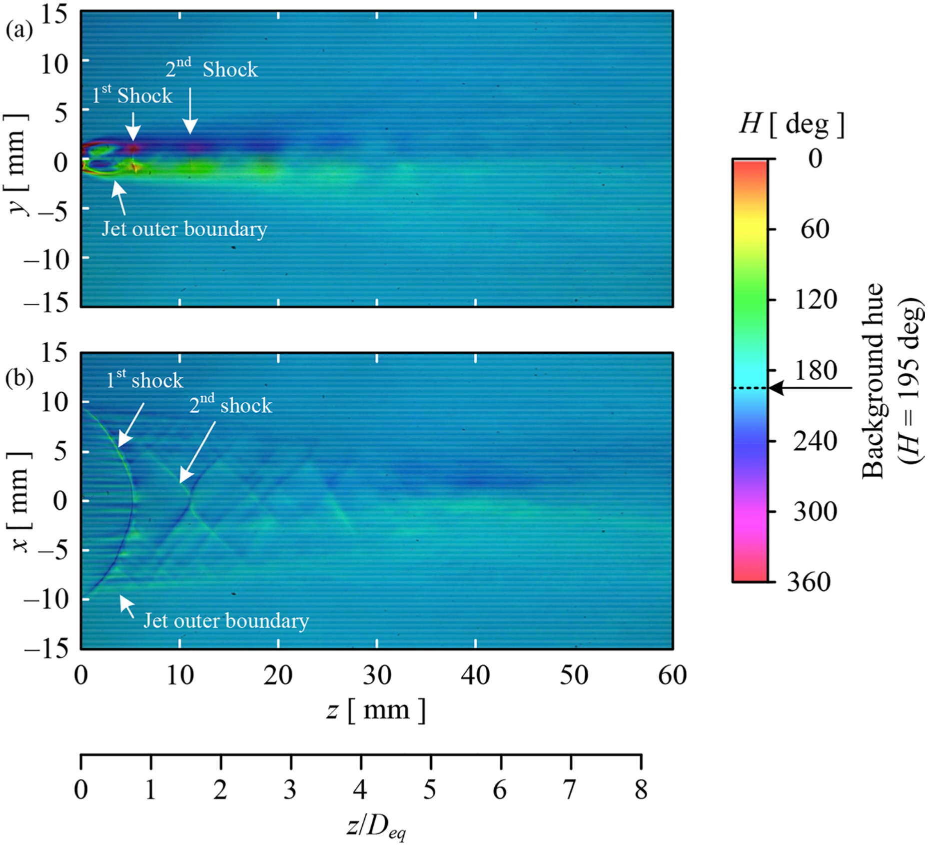

Fig. 5 Rainbow schlieren pictures of an underexpanded elliptic jet taken with horizontal rainbow filter setting for (**a**) the minor-axis plane view and (**b**) the major-axis plane view

cent shape from the nozzle exit lip toward the center axis of the jet. The second shock can be observed immediately after the first shock. However, it is not possible to determine the exact shape from this schlieren image. The jet boundary in the major-axis plane view gradually decreases in the downstream direction toward the jet centerline from just after the nozzle exit. It should be kept in mind that the rainbow schlieren images in Fig. 5 demonstrate the result of averaging the density gradient perpendicular to the jet axis in the viewing direction.

Rao et al. (Rao et al. 2020) investigated the unsteady characteristics of underexpanded jets from an elliptic converging nozzle with an aspect ratio of approximately 8 using high-speed schlieren photography. Their results indicate that the jet exhibits flapping motion in the minor-axis plane, while remaining nearly steady in the major-axis plane. Additionally, the flow oscillations become more intense further downstream. Therefore, the jet becomes blurred beyond the second shock in the schlieren image shown in Fig. 5, indicating a high degree of flow unsteadiness.

3.2 Isopycnic Surface

Figure 6 presents a three-dimensional density field of the shock-containing elliptic jet, depicted using isopycnic representation. This surface is defined as a surface that connects points in a fluid where the density is the same. Specifically, isopycnic surfaces where ρ/ρ_b equals 1.2, 1.6, 1.9, and 2.4 are shown in blue, green, yellow, and red, respectively. Menon and Skews (Menon and Skews 2010), along with Nagata et al. (Nagata et al. 2024), introduced the jet sonic boundary to characterize underexpanded jets. At the sonic boundaries of the jet, the Mach number of the flow is equal to unity, which corresponds to $\rho/\rho_b = 1.2$ at the isopycnic surface (Nagata et al. 2024).

As seen from Fig. 6, the jet density field exhibits a complex three-dimensional structure immediately after the nozzle exit. The jet sonic boundary near the nozzle exit is elliptic in shape, featuring a long major axis and a short minor axis. However, further downstream from the nozzle exit, the lengths of the jet sonic boundaries in the major and minor axis directions become equal, and the cross-sectional shape approaches a circular form. Nagata et al. (Nagata et al. 2024) reported that the structure of the underexpanded jet emerging from an elliptic nozzle with an AR of 4 exhibits an axis-switching phenomenon, where the lengths of the jet sonic boundaries in the major and minor axis directions reverse by 90° as the flow progresses downstream from the nozzle exit. However, the axis-switching phenomenon does not occur in the present experiment. Furthermore, while the studies by Menon and Skews (Menon and Skews 2010), as well as Nagata et al. (Nagata et al. 2024), found that the jet sonic boundaries change continuously in the flow direction, our current study reveals that the jet sonic boundaries are discontinuous downstream. Detailed variations in the flow direction of the jet sonic boundaries in both the minor-axis and major-axis planes are discussed in Sect. 3.3.

3.3 Density Contour Plots

The density contour plots of the underexpanded elliptic jet are shown in Fig. 7, with the flow from left to right. The density field is normalized by the ambient density (ρ_b). The origin of the coordinate system is the center of the cross section at the nozzle exit. The abscissa is the streamwise distance (z) and ordinates denote the vertical distance (y) along the minor-axis and the horizontal distance (x) along the major-axis. The contour level is represented by a

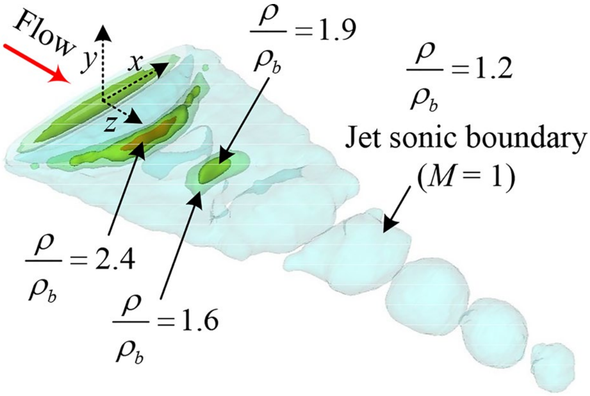

Fig. 6 Isopycnic surface of the underexpanded elliptic jet with $\rho/\rho_b = 1.2$ in blue, 1.6 in green, 1.9 in yellow, and 2.4 in red. The flow Mach number is unity at the jet sonic boundary showing $\rho/\rho_b = 1.2$

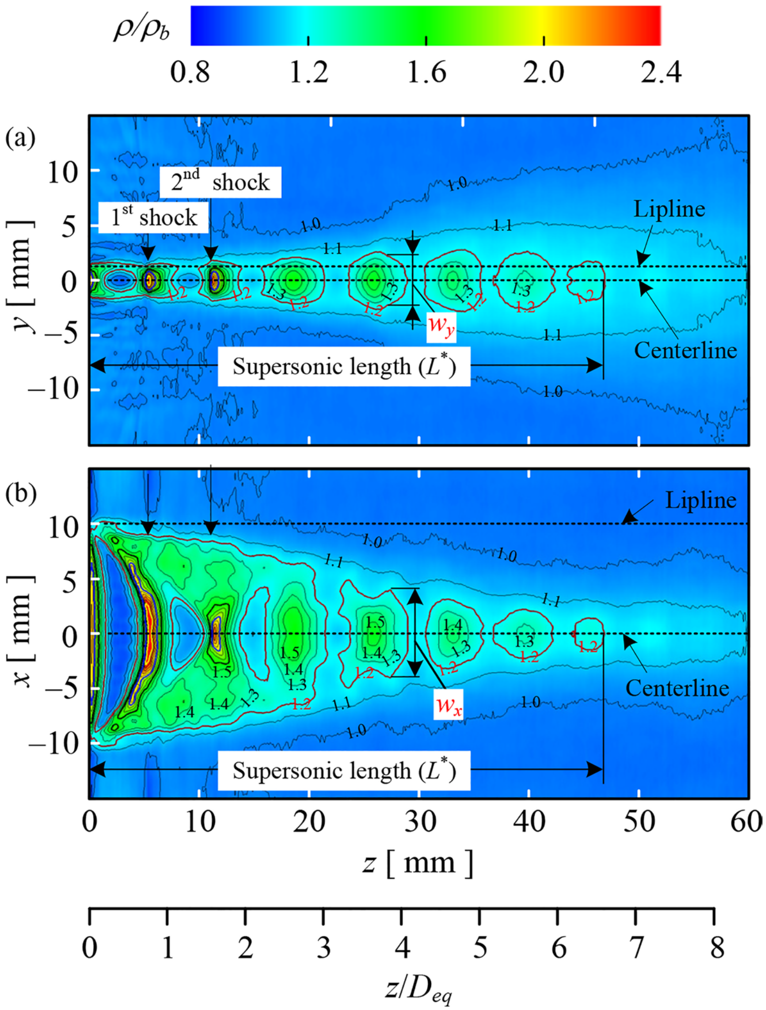

Fig. 7 Density contour plots in the (**a**) minor-axis and (**b**) major-axis planes of the underexpanded elliptic jet. The isodensity lines are drawn at intervals of $\Delta\rho/\rho_b = 0.1$, with the isodensity lines corresponding to mach number equal to unity specifically highlighted in red

color bar at the top of Fig. 7 as a range from a minimum value of 0.8 to a maximum value of 2.4. Isodensity lines are drawn at intervals of $\Delta\rho/\rho_b = 0.1$. The flow Mach numbers reach unity on the lines where $\rho/\rho_b = 1.2$ (Nagata et al. 2024), and these contours are depicted in red. The dashed lines parallel to the abscissa indicate the centerline and lipline. The downward arrows denote the shock locations at the centerline. In Fig. 7(a), almost normal shocks can be observed as the first and second shocks. The length in the flow direction from the nozzle exit to the position sufficiently downstream where the sonic line is unity is called the supersonic length (L^*) (Tashiro et al. 2023). In this experiment, the dimensionless supersonic length is $L^*/D_{eq} = 6.6$.

It is undoubtedly interesting to compare the supersonic length obtained from experiments with different ARs and past empirical formulas. Nagata et al. (Nagata et al. 2024) demonstrated that under the same pressure condition (NPR = 4.0) as in this experiment, the supersonic length of the underexpanded elliptic jet with an AR of 4 is L^*/D_{eq} = 8.4. It indicates that as the AR increases from 4 to 8, the L^*/D_{eq} decreases by approximately 21%. Additionally, the semi-empirical formula for L^*/D_{eq} is given (Nagata et al. 2024) by

$$\frac{L^*}{D_{eq}} = \frac{e^{0.154M_j^2}}{\sqrt{\mathrm{AR}}}\left(-0.226\mathrm{NPR}^2 + 2.87\mathrm{NPR} + 0.03\right) \tag{1}$$

where M_j is the fully expanded jet Mach number, which depends on NPR and the specific heat ratio γ as follows:

$$M_j = \sqrt{\frac{2}{\gamma - 1}\left(\mathrm{NPR}^{\frac{\gamma-1}{\gamma}} - 1\right)} \tag{2}$$

Note that Eq. (1) is reformulated from the original equation of Perumal and Rathakrishnan (Perumal and Rathakrishnan 2021), as organized by Nagata et al. (Nagata et al. 2024) for easier application. When NPR is the same, Eq. (1) suggests that L^*/D_{eq} is inversely proportional to the square root of AR. The normalized supersonic length predicted using Eqs. (1) with (2) is approximately L^*/D_{eq} = 4.1 for γ = 1.4, which is 38$\%$ shorter than the experimental value.

In Fig. 7(b), a crescent-shaped shock can be seen originating from the nozzle exit lip and extending toward the central axis of the jet. It can be slightly confirmed from the concentration of the contour lines that a second shock exists immediately downstream of the first shock. The width between the upper and lower jet outer boundaries decreases slowly in the flow direction from the nozzle exit. In our previous experimental study (Nagata et al. 2024) using an elliptic convergent nozzle of AR = 4 under a pressure condition of NPR = 4, the first shock in the major-axis plane becomes a Mach shock consisting of an incident shock, a reflected shock, and a Mach stem, forming a distinct slip line. However, a Mach stem can not be recognized in Fig. 7(b).

Comparing the density field shown in Fig. 7 with that of the underexpanded elliptic jet of AR = 4 (Nagata et al. 2024), it is observed that in the former, the isodensity lines where the Mach number equals unity exist as multiple closed curves. In contrast, in the latter, these lines form a single, continuous, closed curve extending from the nozzle exit to a considerable downstream distance.

Figure 8 illustrates the streamwise variations of the jet sonic boundary (Nagata et al. 2024). The red and blue solid lines indicate the widths (w_x, w_y) of the jet sonic boundaries in the major-axis and minor-axis planes, respectively, as exemplified in the density field in Fig. 7. In the major-axis plane, w_x initially decreases gradually in the flow direction immediately after the nozzle exit, but it abruptly drops to zero at a position where z/D_{eq} is approximately 3. Subsequently, w_x rises sharply, forming two peaks before dropping to zero again. Afterward, w_x exhibits a mountain-like shape three times before stabilizing at zero. On the other hand, w_y initially remains almost constant from the nozzle exit with increasing distance and then abruptly drops to zero at z/D_{eq} = 1, forming six mountain-like shapes. The distribution of the last three mountain-like shapes of w_x and w_y nearly overlap.

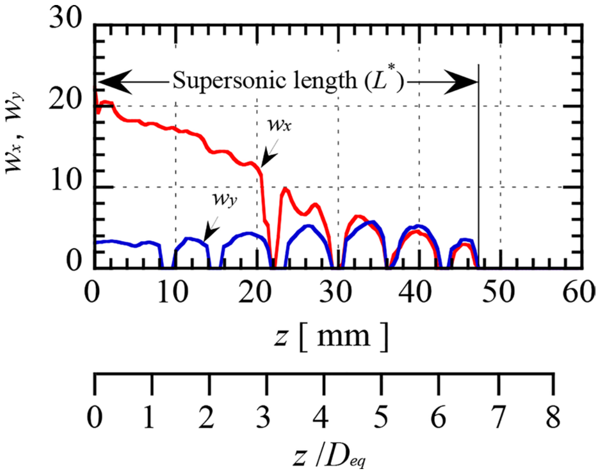

Fig. 8 Streamwise variations in the widths (w_x, w_y) of the jet sonic boundaries in the minor-axis and major-axis planes of the underexpandedelliptic jet

An important point here is that w_y never exceeds w_x. This indicates that the axis-switching phenomenon, which occurs in the underexpanded elliptic jet with an AR of 4 (Nagata et al. 2024), does not occur. This can also be qualitatively observed from the three-dimensional density field of the jet shown in Fig. 6.

3.4 Streamwise Density Distributions

Typical density distributions along (a) the jet centerline, (b) the lipline in the minor-axis plane, and (c) the lipline in the major-axis plane are depicted in Fig. 9 as blue solid lines. Uncertainty error bars are added in red to each density distribution. The study by Sugawara et al. (Sugawara et al. 2020) on shock-containing round microjets demonstrates that bias errors are negligibly small compared to random errors. Therefore, the error bars in Fig. 9 do not include bias errors. In addition, to avoid clutter, the error bars are displayed at appropriate intervals along the flow direction. Details on the error evaluation method are described in our previous paper (Nagata et al. 2024). In Figs. 9(a)~(c), the average measurement uncertainties are 1.4%, 0.79%, and 0.42% of ρ_b, respectively.

The vertical axis denotes the density normalized by the ambient density and horizontal axis is the streamwise distance from the nozzle exit. The leftward arrow on the vertical axis denotes the theoretical density ratio at the nozzle exit, which is calculated under the assumption of isentropic flow from the nozzle inlet to the exit. In addition, the supersonic length is marked by short green line. Furthermore, the dashed line parallel to the horizontal axis in Fig. 9 shows the normalized density ($\rho_j/\rho_b = 1.49$) at the jet free boundary, where the static pressure is the same as the back pressure (p_b), but the density is different from the ambient density (Sugawara et al. 2020).

As shown in Fig. 9(a), the experimental density ratio at the nozzle exit is approximately 2.2, which is lower than the theoretical value of 2.54. This is due to the effect of light reflection at the nozzle exit cross-section. At around 3 mm downstream of the nozzle exit, the density in the jet rapidly decreases to 92% of the atmospheric density, and the theoretical Mach number at this position is predicted to be about $M_1 = 2.0$, assuming an isentropic change. The maximum Mach number in underexpanded jets emerging from a convergent nozzle can

Fig. 9 Streamwise density profiles with uncertainty error bars along the (**a**) jet centerline, (**b**) lipline in the minor-axis plane, and (**c**) lipline in the major-axis plane

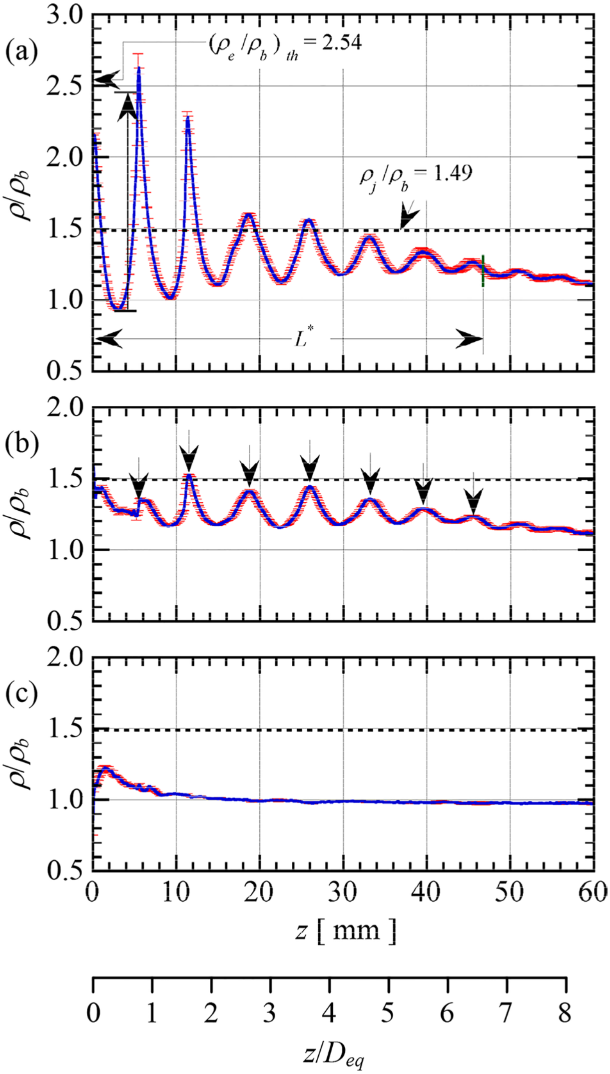

be predicted to occur at the first minimum of the density or static pressure distribution on the jet central axis. For reference, Tashiro et al. (Tashiro et al. 2023) proposed an experimental relation given by

$$M = 1 + 0.72\ (\mathrm{NPR} - 1.89)^{0.76} \tag{3}$$

for the Mach number obtained from the first minimum value in the density profile along the central axis of underexpanded jets issuing from a circular convergent nozzle. Substituting NPR=4 into Eq. (3) gives a Mach number of approximately 2.3, which is approximately 15% larger when compared to the present experimental result. The effects of AR and NPR on the maximum Mach number inside the shock-containing elliptic jets are left for future research.

In the density distribution along the jet centerline, the streamwise locations of the local density maxima correspond approximately to those of the shocks. The values of the local density maxima are largest at the location of the first shock, which is attributed to the strength of the shock. The initial value of the density peaks is the highest and diminish as they move downstream, whereas the initial value of the density minima is the lowest and progressively rise downstream.

The distance between the streamwise locations of the first and second density maxima indicates the shock-cell length (L_s) (Tashiro et al. 2023). The L_s/D_{eq} is determined to be 0.82 from the density profile along the jet centerline in Fig. 9(a). This value is approximately 13% lower than the analytical value of 0.94 predicted using the previous flow model (Nagata et al. 2022).

There are no other experimental values comparable to the present data for the density field within the shock-containing elliptic jet. However, theoretical predictions can be made for the density increase caused by the first shock, since it can be approximated as a normal shock near the jet centerline. Using a freestream Mach number of $M_1 = 2.0$ just before the first shock, the post-shock density can be determined using the Rankine-Hugoniot relations. In Fig. 9(a), the theoretical density increment due to the first shock is indicated by an upward arrow with two short horizontal bars. The density ratio across the first shock, obtained from the density profile along the jet centerline, agrees with the theoretical value for the normal shock within approximately 7% and hence, the theoretical value is of the same order of magnitude as the experimental value.

Figure 9(b) presents the density distribution along the lipline in the minor-axis plane. The downward arrows in the figure indicate the positions of the density peaks. A comparison between Figs. 7(a) and 9(b) suggests that the lipline traverses the jet sonic boundaries, implying that the density peaks occur at the locations of the shocks within these boundaries. On the other hand, as shown by comparing Figs. 7(b) and 9(c), the lipline in the major-axis plane lies outside the jet, resulting in the density along this line being equal to the atmospheric density at all locations.

3.5 Shock Structures and Topology

Shock structures and topology, including the spatial evolution of shock waves, shock-to-shock interactions, and shock reflection and diffraction, can be quantitatively expressed through the magnitude of the density gradient vector, represented by

$$\frac{D_{eq}}{\rho_b}\left|\nabla\rho\right| = \frac{D_{eq}}{\rho_b}\sqrt{\left(\frac{\partial\rho}{\partial x}\right)^2 + \left(\frac{\partial\rho}{\partial y}\right)^2 + \left(\frac{\partial\rho}{\partial z}\right)^2} \tag{4}$$

in nondimensional form. This quantity indicates the degree of compression and expansion in all directions. Such representation effectively highlights the shapes of shock waves and the locations where expansion waves begin (Sugawara et al. 2020).

Figure 10 illustrates the three-dimensional structure of the first and second shocks within the underexpanded elliptic jet of AR = 8. Nagata et al. (Nagata et al. 2024) experimentally demonstrated that the first shock within the underexpanded elliptical jet of AR = 4 consists of three components: an incident shock, Mach stem, and reflected shock. On the other hand,

Fig. 10 Three-dimensional shock structures of the underexpanded elliptic jet with an aspect ratio of 8

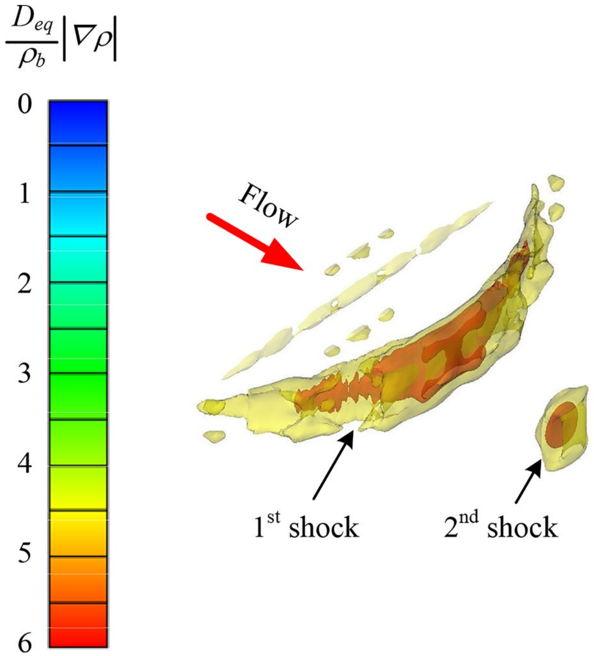

as shown in Fig. 10, the first shock within the underexpanded elliptic jet of AR = 8 has a crescent shape, and no reflected shock is formed. Additionally, it is observed that the strength of the crescent-shaped shock decreases radially from the center of the jet. The second shock is significantly smaller compared to the first shock, and its central part has a circular shape.

3.6 Effects of Angular Step

It is essential to investigate how the size of the angular step affects the reconstructed density field. Smaller angular steps yield greater accuracy but require longer experimental times and larger volumes of data. Therefore, it is ideal to keep the angular step as small as possible. However, to the best of the author's knowledge, no studies have been conducted on the effect of the angular step on the reconstructed density field in the context of applying rainbow schlieren tomography to supersonic flow.

The jet density fields were reconstructed by varying the angular step ($\Delta\theta$) to 5°, 10°, 20°, and 30°. Figure 11 shows the effect of the $\Delta\theta$ on the density field in the minor-axis plane. The density distributions corresponding to $\Delta\theta$ at 5°, 10°, 20°, and 30° are represented by blue, yellow, green, and red, respectively. It can be seen that the overall structure of the density field, including the shape of the shock-cells and the jet boundaries, is not significantly affected by the $\Delta\theta$. However, in the region where the first and second shocks occur, some spurious contributions can be observed extending outward from the center of the jet, and this effect becomes more pronounced with increasing $\Delta\theta$.

Figure 12 shows the effect of the $\Delta\theta$ on the density field in the major-axis plane. Similar to the density field in the minor-axis plane, spurious contributions are observed at the jet boundaries where the first and second shocks are produced. In particular, the density field for $\Delta\theta = 30°$ is markedly different from the other density fields.

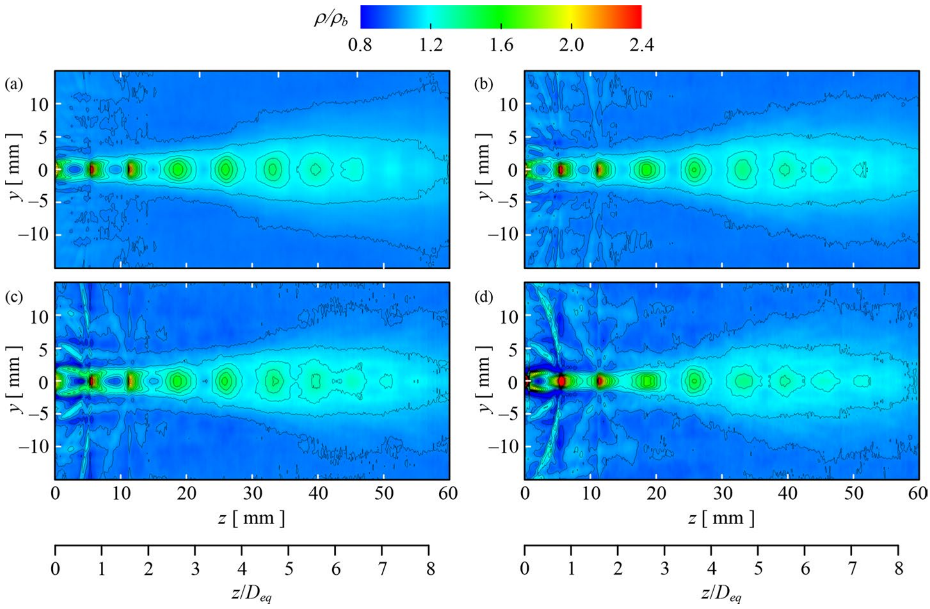

Fig. 11 Effect of the angular step ($\Delta\theta$) on the density contour plots in the major-axis plane for (**a**) $\Delta\theta = 5$ °, (**b**) $\Delta\theta = 10$ °, (**c**) $\Delta\theta = 20$ °, and $\Delta\theta = 30$ °

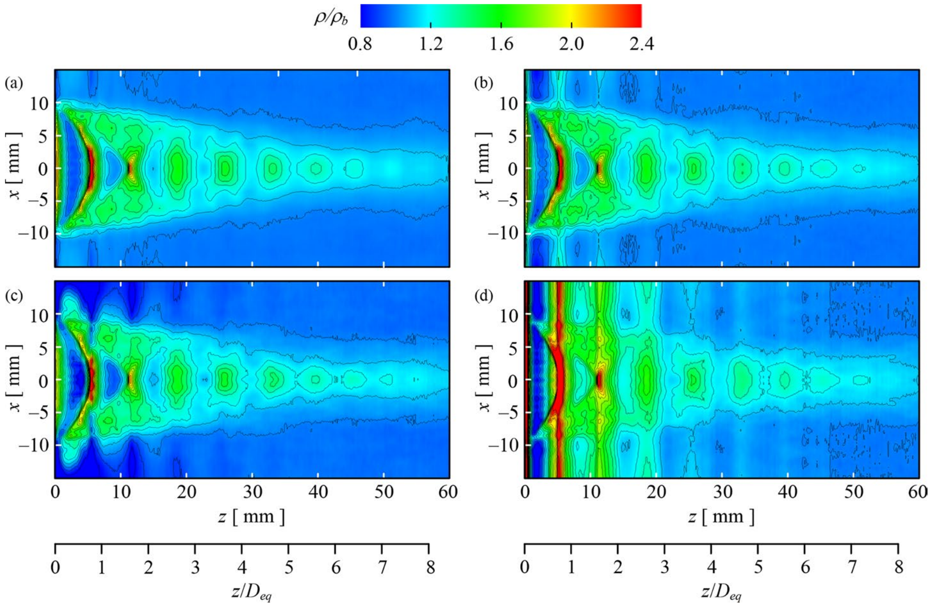

Fig. 12 Effect of the angular step ($\Delta\theta$) on the density contour plots in the minor-axis plane for (**a**) $\Delta\theta = 5°$, (**b**) $\Delta\theta = 10°$, (**c**) $\Delta\theta = 20°$, and $\Delta\theta = 30°$

Fig. 13 Effect of the angular step on the streamwise density profiles along (**a**) the jet centerline, (**b**) the lipline in the minor-axis plane, and (**c**) the lipline in the major-axis plane

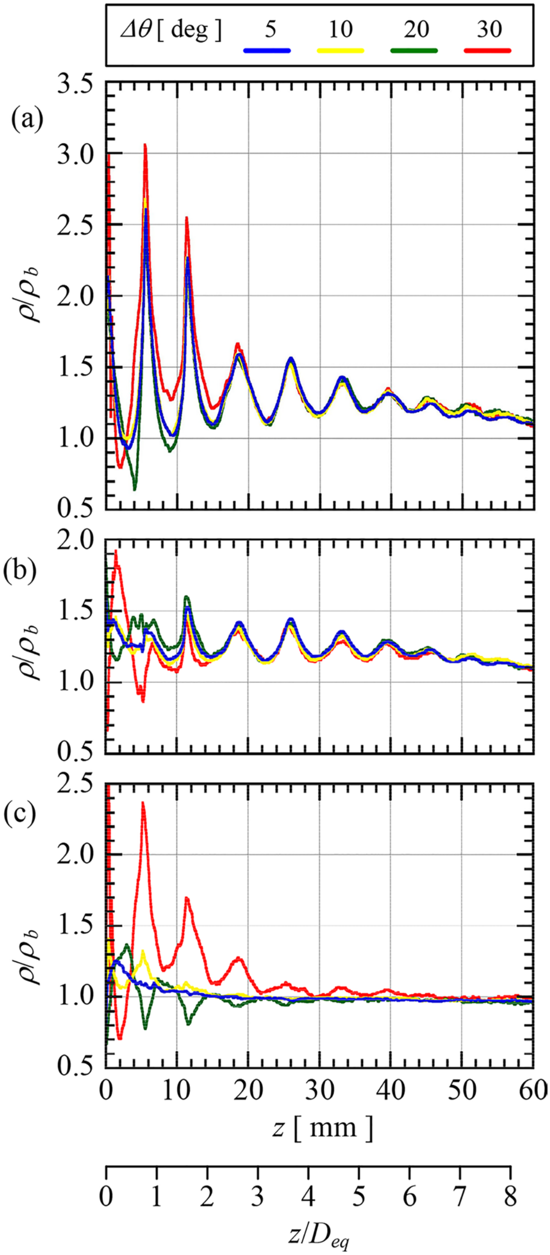

To quantitatively evaluate the effect of the $\Delta\theta$ on the density field, Fig. 13 demonstrates the density distributions along three representative flow directions: (a) the jet centerline, (b) the lipline in the minor-axis plane, and (c) the lipline in the major-axis plane. First, attention is directed to the density distribution along the jet centerline. The density increases due to the first and second shocks are similar for $\Delta\theta_s$ from 5° to 20°, but for $\Delta\theta = 30°$, the density increase is significantly higher compared to that for $\Delta\theta = 5°$. Regarding the minimum density values just before the first and second shocks, the density distributions for $\Delta\theta = 5^\circ$ and 10° are similar, but the distributions for $\Delta\theta = 20^\circ$ and 30° show a larger deviation compared to that for $\Delta\theta = 5^\circ$. Downstream of the second shock, the effect of the $\Delta\theta$ on the density distribution is minimal. Next, Fig. 13(b) is examined to observe the effect of $\Delta\theta$ on the density distribution along the lipline in the minor-axis plane. In the region from the nozzle exit to approximately $z/D_{eq} = 1$, the density distribution for $\Delta\theta = 30^\circ$ is markedly different from the other distributions. However, downstream of approximately $z/D_{eq} = 1$, the effect of the $\Delta\theta$ on the density distribution is negligible. Finally, Fig. 13(c), which shows the density distribution along the lipline in the major-axis plane, is examined. Downstream of approximately $z/D_{eq} = 1$, the density distributions for $\Delta\theta = 5^\circ$ and 10° quantitatively match well. The density distribution for $\Delta\theta = 20^\circ$ shows good quantitative agreement with that for $\Delta\theta = 5^\circ$ downstream of approximately $z/D_{eq} = 2$. The density distribution for $\Delta\theta = 30^\circ$ is markedly different from that for $\Delta\theta = 5^\circ$ from the nozzle exit to approximately $z/D_{eq} = 3$. However, downstream of approximately $z/D_{eq} = 3$, it shows reasonable quantitative agreement with the density distribution for $\Delta\theta = 5^\circ$.

4 Conclusions

Rainbow schlieren tomography (RST) was used to obtain the three-dimensional density field of an underexpanded jet emerging from an elliptic convergent nozzle with an aspect ratio (AR) of 8. The detailed flow features in the shock-dominated region of the underexpanded elliptic jet were then quantitatively resolved at a spatial resolution of 13 μm. The conclusions obtained in the present study are as follows.

(1) The isopycnic surface of the underexpanded elliptic jet shows that the jet sonic boundary near the nozzle exit has an elliptic shape, which transitions to a circular form further downstream as the lengths of the jet sonic boundaries in the major and minor axis directions become equal. In addition, the jet sonic boundaries have multiple closed isodensity lines. No axis-switching phenomenon occurs.

(2) The supersonic length (L^*) normalized by the equivalent diameter (D_{eq}) is $L^*/D_{eq} = 6.6$ for the underexpanded elliptic jet of AR = 8. A comparison with a previous experimental study for AR = 4 shows that when AR increases from 4 to 8, L^*/D_{eq} decreases by approximately 21%. The semi-empirical formula using Eqs. (1) with (2) predicts $L^*/D_{eq} = 4.1$, which is 38% shorter than the present experimental value.

(3) The density profiles along the jet centerline, as well as the liplines in the minor-axis and major-axis planes, exhibit uncertainty errors of 1.4%, 0.79%, and 0.42%, respectively, relative to the ambient density. The experimental density ratio across the first shock, derived from the density profile along the jet centerline, aligns with the theoretical value for the normal shock within an approximate margin of 7%.

(4) The first shock within the underexpanded elliptic jet exhibits a crescent shape without a reflected shock, and its strength diminishes from the jet's center outward, while the second shock is notably smaller than the first shock, with a circular central part.

(5) The jet density fields were reconstructed with angular steps ($\Delta\theta_s$) of 5°, 10°, 20°, and 30°. In the minor-axis plane, the overall structure of the density field, including shock-cells and jet boundaries, remains largely unaffected by the $\Delta\theta$. Nonetheless, spurious

contributions, particularly in the first and second shock regions, increases with larger $\Delta\theta_s$. In the major-axis plane, the density field for $\Delta\theta=30°$ differs significantly from others. Therefore, $\Delta\theta$ must be set to a value below 30° at minimum.

(6) The effects of $\Delta\theta$ on the streamwise density profiles were examined. For the density profile along the jet centerline, the density rise due to the first shock is consistent for $\Delta\theta_s$ from 5° to 20°, but significantly higher for $\Delta\theta=30°$. Minimum density values before the first and second shocks are similar for $\Delta\theta=5°$ and 10°, with larger deviations at $\Delta\theta=20°$ and 30°. Downstream of the second shock, the effect of $\Delta\theta$ is minimal. Along the lipline in both minor and major-axis planes, the density profile for $\Delta\theta=30°$ shows marked differences between the nozzle exit and z/D_{eq}=around 3, but is reasonably well downstream of z/D_{eq}=around 3.

It should be noted that the conclusions drawn in this study are limited to underexpanded elliptical jets with aspect ratios not exceeding 8. The experimental data provided in this study are expected to offer valuable insights for validating numerical simulations and developing analytical models related to shock-containing elliptical jets.

Acknowledgements The authors would like to thank Dr. Takeshi Miyaguni of the University of Kitakyushu for the fabrication of the test nozzle using the 3D printer.

Author Contribution SN and YM contributed to the conceptualization; TS contributed to the data curation, formal analysis, and visualization; TS and TN contributed to the investigation; TS contributed to the software; SN contributed to the resources and project administration; SN and YM contributed to the supervision; TS and TN contributed to the validation; and TS and YM wrote the main manuscript text. All authors reviewed the manuscript.

Funding This work was supported in part by a Grant-in-Aid for Scientific Research(C) (Grant No. 20K04272).

Data Availability No datasets were generated or analysed during the current study.

Declarations

Ethics Approval and Consent to Participate Not applicable.

Competing Interests The authors declare no competing interests.

References

Agrawal, A.K., Wanstall, C.T.: Rainbow schlieren deflectometry for scalar measurements in fluid flows. J. Flow Vis. Image Process. **25**(3–4), (2018)

Edgington-Mitchell, D.: Aeroacoustic resonance and self-excitation in screeching and impinging supersonic jets - a review. Int. J. Aeroacoust. **18**(2–3), 118–188 (2019)

Edgington-Mitchell, D., Honnery, D.R., Soria, J.: Multimodal instability in the weakly underexpanded elliptic jet. AIAA J. **53**(9), 2739–2749 (2015a)

Edgington-Mitchell, D., Honnery, D.R., Soria, J.: Staging behavior in screeching elliptical jets. Int. J. Aeroacoust. **14**(7), 1005–1024 (2015b)

Feng, T., McGuirk, J.J.: Measurements in the annular shear layer of high subsonic and under-expanded round jets. Exp. Fluids **57**(1), 7 (2016)

Fukunaga, R., Ezoe, M., Nakao, S., Miyazato, Y.: Application of rainbow schlieren tomography for shock-containing rectangular jets. J. Vis. **25**(4), 687–695 (2022)

Islam, M.M., Nagata, T., Nakao, S., Miyazato, Y.: Theoretical study of slightly underexpanded jets from elliptical nozzles. Trans. Japan Soc. Aeronaut. Space. Sci. **67**(1), 32–39 (2024)

Ivelja, R., Edgington-Mitchell, D., Maigler, M., Petrônio, A.S.N.: Modal analysis of screeching elliptical jets. J. Fluid Mech. **1000**, 68 (2024)

Katanoda, H., Miyazato, Y., Masuda, M., Matsuo, K.: Pitot pressures of correctly-expanded and underexpanded free jets from axisymmetric supersonic nozzles. Shock Waves **10**, 95–101 (2000)

Kinzie, K., McLaughlin, D.K.: Aeroacoustic properties of supersonic elliptic jets. J. Fluid Mech. **395**, 1–28 (1999)

Kolhe, P.S., Agrawal, A.K.: Density measurements in a supersonic microjet using miniature rainbow schlieren deflectometry. AIAA J. **47**(4), 830–838 (2009)

Léon, O., Donjat, D., Olchewsky, F., Desse, J.-M., Nicolas, F., Champagnat, F.: Three-dimensional density field of a screeching under-expanded jet in helical mode using multi-view digital holographic interferometry. J. Fluid Mech. **947**, 36 (2022)

Li, X., Zhou, R., Yao, W., Fan, X.: Flow characteristic of highly underexpanded jets from various nozzle geometries. Appl. Therm. Eng. **125**, 240–253 (2017)

Maeda, H., Fukuda, H., Kubo, K., Nakao, S., Ono, D., Miyazato, Y.: Structure of underexpanded supersonic jets from axisymmetric Laval nozzles. J. Flow Vis. Image Process. **25**(1), (2018)

Mazharmanesh, S., Petrônio, A.S.N., Weightman, J., Edgington-Mitchell, D.: Manifestation of screech modes in non-axisymmetric jets. J. Fluid Mech. **1004**, 7 (2025)

Menon, N., Skews, B.W.: Shock wave configurations and flow structures in non-axisymmetric underexpanded sonic jets. Shock Waves **20**, 175–190, (2010)

Mitchell, D.M., Honnery, D.R., Soria, J.: Near-field structure of underexpanded elliptic jets. Exp. Fluids **54**, 1578 (2013)

Nagata, T., Islam, M.M., Miyaguni, T., Nakao, S., Miyazato, Y.: Shock-cell spacings of underexpanded sonic jets emerging from elliptic nozzles. Exp. Fluids **63**(7), 111 (2022)

Nagata, T., Sakashita, T., Nakao, S., and Miyazato, Y.: Three-dimensional flow features of underexpanded jets emerging from an elliptic convergent nozzle. Exp. Fluids **65**(10), 146 (2024)

Perumal, A.K., Rathakrishnan, E.: Scaling law for supersonic core length in circular and elliptic free jets. Phys. Fluids **33**(5), (2021)

Rao, A.N., Kushari, A., Chandra Mandal, A.: Screech characteristics of under-expanded high aspect ratio elliptic jet. Phys. Fluids **32**(7), 076106 (2020)

Sakashita, T., Nagata, T., Nakao, S., Miyazato, Y.: Quantitative flow visualization of an elliptic underexpanded sonic jet by RST. In: The Proceedings of the 8th International Conference on Jets, Wakes and Separated Flows, The Japan Society of Mechanical Engineers (2024)

Sakurai, T., Handa, T., Koike, S., Mii, K., Nakano, A.: Study on the particle traceability in transonic and supersonic flows using molecular tagging velocimetry. J. Vis. **18**, 511–520 (2015)

Settles, G.S.: Schlieren and Shadowgraph Techniques: visualizing Phenomena in Transparent Media. Springer-Verlag, Berlin Heidelberg New York (2001)

Settles, G.S., Hargather, M.J.: A review of recent developments in schlieren and shadowgraph techniques. Meas. Sci. Technol. **28**(4), 042001 (2017)

Sugawara, S., Nakao, S., Miyazato, Y., Ishino, Y., Miki, K.: Three-dimensional reconstruction of a microjet with a mach disk by Mach-Zehnder interferometers. J. Fluid Mech. **893**, 25 (2020)

Sugawara, S., Nakao, S., Miyazato, Y., Ishino, Y., Miki, K.: Quantitative flow visualization of slightly underexpanded microjets by Mach-Zehnder interferometers. Flow Turbul. Combust. **106**(3), 971–992 (2021)

Takano, H., Kamikihara, D., Ono, D., Nakao, S., Yamamoto, H., Miyazato, Y.: Three-dimensional rainbow schlieren measurements in underexpanded sonic jets from axisymmetric convergent nozzles. J. Therm. Sci. **25**(1), 78–83 (2016)

Tashiro, T., Fukunaga, R., Utsunomiya, D., Nakao, S., Miyazato, Y., Ishino, Y.: Flow features of underexpanded microjets emerging from a round convergent nozzle. Exp. Fluids **64**(3), 55 (2023)

Yoo, J., Mitchell, D., Davidson, D.F., Hanson, R.K.: Planar laser-induced fluorescence imaging in shock tube flows. Exp. Fluids **49**, 751–759 (2010)

Yoshimi, S., Yamashita, T., Nakao, S., Miyazato, Y.: Near-field flow features of underexpanded microjets emerging from a rectangular convergent nozzle with a high-aspect-ratio. Flow Meas. Instrum. 102945 (2025)

Yüceil, K.B.: A comparison of piv and interferometric rayleigh scattering measurements in the near field of underexpanded sonic jets. Aerosp. Sci. Technol. **67**, 31–40 (2017)